

Relaxation of a 1-D gravitational system

P. Valageas

Service de Physique Théorique, CEA Saclay, 91191 Gif-sur-Yvette, France

(Dated: May 25, 2019)

We study the relaxation towards thermodynamical equilibrium of a 1-D gravitational system. This OSC model shows a series of critical energies E_{cn} where new equilibria appear and we focus on the homogeneous ($n = 0$), one-peak ($n = \pm 1$) and two-peak ($n = 2$) states. Using numerical simulations we investigate the relaxation to the stable equilibrium $n = \pm 1$ of this N -body system starting from initial conditions defined by equilibria $n = 0$ and $n = 2$. We find that in a fashion similar to other long-range systems the relaxation involves a fast violent relaxation phase followed by a slow collisional phase as the system goes through a series of quasi-stationary states. Moreover, in cases where this slow second stage leads to a dynamically unstable configuration (two peaks with a high mass ratio) it is followed by a new sequence “violent relaxation/slow collisional relaxation”. We obtain an analytical estimate of the relaxation time $t_{2 \rightarrow \pm 1}$ through the mean escape time of a particle from its potential well in a bistable system. We find that the diffusion and dissipation coefficients satisfy Einstein’s relation and that the relaxation time scales as $Ne^{1/T}$ at low temperature, in agreement with numerical simulations.

PACS numbers: Valid PACS appear here

I. INTRODUCTION

The thermodynamics and dynamics of systems with long-range interactions have been the focus of many studies in recent years [1]. Indeed, such systems exhibit many peculiar features due to their long-range nature and non-additivity, such as ensemble inequivalence between micro-canonical, canonical and grand-canonical ensembles and regions of negative specific heat [2]. On the other hand, their dynamics presents many interesting phenomena [3]. In particular, the relaxation to thermodynamical equilibrium can be very slow and diverge with the number N of particles [4, 5, 6]. Moreover, it often proceeds in two steps with greatly different time-scales. Thus, there is first a collisionless relaxation over a few dynamical times which involves collective dynamical instabilities. This step is also called violent relaxation in astrophysics [7]. Then, after the system has reached a mean-field equilibrium a collisional relaxation associated with two-body encounters, or more generally due to the discrete nature of the matter distribution which gives rise to fluctuations with respect to the smooth mean-field potential (finite N effects), leads to a slow relaxation towards statistical equilibrium over a time-scale which diverges with N [8].

A prototype of such systems with long-range interactions is the Hamiltonian Mean Field (HMF) model defined by a cosine interaction for particles moving on a circle. Then, it has been shown [8] that the system first converges to a stable stationary solution of the mean-field Vlasov equation. Next, the relaxation to thermodynamical equilibrium proceeds over a much longer time-scale through a slowly varying sequence of stable stationary states of the Vlasov dynamics. This also implies that the dynamics of the system strongly depends on the initial conditions since there are an infinite number of stable stationary solutions of the Vlasov equation [8, 9].

In this article we study the relaxation of the 1-D gravitational system described in details in [10]. This One-dimensional Static Cosmology (OSC) model consists of particles moving between two reflecting walls within an external potential V which balances the 1-D gravitational self-interaction Φ so that the homogeneous state (i.e. constant density) is an equilibrium solution. This model also corresponds to the evolution of 1-D density fluctuations in a 3-D cosmological background over time-scales much smaller than the Hubble time so that the expansion of the universe can be neglected. As shown in [10], this system exhibits a series of critical energies E_{cn} ($E_{c1} > E_{c2} > \dots$). At high energies the only stable thermodynamical equilibrium is the homogeneous state (called “ $n = 0$ ”) and at each transition E_{cn} two new thermodynamical equilibria ($\pm n$) appear. Moreover, equilibria ± 1 are stable below E_{c1} (while the homogeneous state turns unstable) whereas other equilibria $\pm n$ with $n \geq 2$ are unstable (both from a thermodynamical and a mean-field dynamical analysis) except for equilibrium $n = 2$ which becomes stable for the Vlasov dynamics just below E_{c2} but remains thermodynamically unstable. In this article we study the relaxation of the OSC model starting from either the $n = 0$ or $n = 2$ equilibria, which allows us to investigate both collisionless and collisional processes. We first recall in sect. II the thermodynamical properties of the OSC model. Next, we study the relaxation of the system, starting from the homogeneous state in sect. III A and starting from equilibrium $n = 2$ in sect. III B. Finally we conclude in sect. IV.

II. THE OSC MODEL

A. Description of the model

The OSC model [10] consists of N particles of mass m which move along the x -axis in the interval $0 < x < L$ (with reflecting walls) within an external concave quadratic potential $V(x)$ and which interact through 1-D gravity. Thus, the Hamiltonian \mathcal{H}_N of the system is:

$$\mathcal{H}_N = m \sum_{i=1}^N \frac{v_i^2}{2} + gm^2 \sum_{i>j} |x_i - x_j| + m \sum_{i=1}^N V(x_i), \quad (1)$$

where $v_i = \dot{x}_i$ is the velocity of particle i (we note by a dot the derivatives with respect to time t), g is the coupling constant of the 1-D gravitational interaction and the external potential $V(x)$ is:

$$V(x) = -g\bar{\rho}[(x - L/2)^2 + L^2/4], \quad (2)$$

where $\bar{\rho} = M/L$ is the mean density of the system ($M = Nm$ is the total mass). In [10] the thermodynamics and stability properties of the OSC system were studied in the mean-field limit (i.e. continuum limit) where the mass m goes to zero at fixed density $\bar{\rho}$. Then, the gravitational self-interaction is described by the potential $\Phi(x)$ with:

$$\Phi(x) = g \int_0^L dx' \rho(x') |x - x'|, \quad (3)$$

and the dynamics of the system is governed by the Vlasov equation for the phase-space density $f(x, v, t)$ within the total potential ϕ :

$$\frac{\partial f}{\partial t} + v \cdot \frac{\partial f}{\partial x} - \frac{\partial \phi}{\partial x} \cdot \frac{\partial f}{\partial v} = 0, \quad \phi = \Phi + V. \quad (4)$$

The main feature of the OSC model which comes from its cosmological context is the appearance of the background potential $V(x)$ which ensures that the homogeneous configuration $\rho = \bar{\rho}$ is a solution of the equations of motion (it is the counterpart of the Hubble flow for the expanding universe). Alternatively, the constant density $\bar{\rho}$ defined from the potential V can be interpreted as a cosmological constant (in which case it is not necessarily equal to the mean matter density) if we work in physical coordinates. The statistical mechanics of such a system has been studied in the 3-D case in [11, 12]. Here, following [10] we interpret the OSC model as derived from a simple cosmological framework without cosmological constant. Then, the external potential V appears through the change to comoving coordinates [13] and the Hamiltonian (1) applies on time-scales which are shorter than the Hubble time (so that the expansion of the universe can be neglected and there is no explicit time dependence in the Hamiltonian (1)). However, for our purposes the OSC model can also be studied for its own sake as a simple model of systems with scale-free long-range interaction which exhibits an interesting behaviour (in particular the

series of critical energies discussed in [10] and recalled below in Eq.(11)). In the following we shall decompose the total energy E from (1) into its kinetic (K), self-gravity ($\bar{\Phi}$) and potential (\bar{V}) components as $E = K + \bar{\Phi} + \bar{V}$ with:

$$K = m \sum_{i=1}^N \frac{v_i^2}{2}, \quad \bar{V} = m \sum_{i=1}^N V(x_i), \quad (5)$$

$$\bar{\Phi} = gm^2 \sum_{i>j} |x_i - x_j| = m \sum_{i=1}^N \frac{\Phi(x_i)}{2}. \quad (6)$$

B. Thermodynamical equilibria

At thermodynamical equilibrium the phase-space density is the usual Maxwell-Boltzmann distribution:

$$f(x, v) = \rho(x) \sqrt{\frac{\beta}{2\pi}} e^{-\beta v^2/2} \propto e^{-\beta[v^2/2 + \phi(x)]}, \quad (7)$$

where we introduced the inverse temperature $\beta = 1/T$. The density is related to the potential by the Poisson equation modified by a constant term due to the background V :

$$\frac{d^2\varphi}{dx^2} = 2g(\rho - \bar{\rho}) \quad \text{with} \quad \phi = \varphi + \bar{\varphi} \quad \text{and} \quad \rho = \bar{\rho} e^{-\beta\varphi}. \quad (8)$$

Here we introduced for convenience the offset $\bar{\varphi}$ defined by the condition $\rho = \bar{\rho}$ for $\varphi = 0$. Therefore, the thermodynamical equilibrium is set by the equations:

$$\frac{d^2\varphi}{dx^2} = 2g\bar{\rho}(e^{-\beta\varphi} - 1) \quad \text{and} \quad \varphi'(0) = \varphi'(L) = 0. \quad (9)$$

The homogeneous state $\rho = \bar{\rho}$ (i.e. $\varphi = 0$) is a solution of Eqs.(9) which we label as “equilibrium $n = 0$ ”. Its total energy is:

$$E_0 = \frac{MT}{2} - \frac{gM^2L}{6}. \quad (10)$$

Note that the energy E_0 is bounded from below by $E_{\min}(0) = -gM^2L/6$. Besides, as shown in [10], Eqs.(9) yield a series of critical temperatures T_{cn} and energies E_{cn} ($n = 1, 2, \dots$) where new thermodynamical equilibria appear, with:

$$T_{cn} = \frac{2gML}{n^2\pi^2}, \quad E_{cn} = -\frac{n^2\pi^2 - 6}{6n^2\pi^2} gM^2L. \quad (11)$$

Thus, at high temperatures above T_{c1} the only thermodynamical equilibrium is the homogeneous solution $\rho = \bar{\rho}$ ($n = 0$). Below T_{c1} this state becomes unstable and two new stable equilibria “ $n = \pm 1$ ” appear. The state $n = 1$ corresponds to a density peak at $x = 0$ and a density minimum at $x = L$, whereas the state $n = -1$ is its reflection through $x = L/2$. Similarly, at each critical temperature T_{cn} two new equilibria $\pm n$ appear, which consist of n

half-oscillations (i.e. from a density peak to a density minimum). The state $n > 0$ shows a peak at $x = 0$ whereas the state $n < 0$ shows a minimum at $x = 0$. As described in [10] the OSC model can also be extended to the whole real line by symmetry with respect to $x = 0$ and periodicity of $2L$. Then, state $n < 0$ is a mere translation of state $|n|$ by $L/|n|$. Thus, the equilibrium $n = 2$ displays a density peak at each boundary $x = 0, L$ and a minimum at $x = L/2$ (whereas state $n = -2$ shows one density peak at $x = L/2$ and two density minima at $x = 0, L$). Moreover, all thermodynamical equilibria $\pm n$ can be obtained from state $n = 1$ at a rescaled temperature:

$$\rho_n(\zeta; \beta) = \rho_1(\zeta; \frac{\beta}{n^2}), \quad \rho_{-n}(\zeta; \beta) = \rho_1(\zeta - \frac{\zeta_L}{n}; \frac{\beta}{n^2}), \quad (12)$$

where we wrote explicitly the dependence on inverse temperature β and we defined the dimensionless coordinate ζ by:

$$\zeta = \frac{x}{L_J} = \zeta_L \frac{x}{L} \quad \text{with} \quad L_J = \frac{1}{\sqrt{2g\bar{\rho}\beta}}, \quad \zeta_L = \frac{L}{L_J}, \quad (13)$$

where we introduced the ratio ζ_L of the system size L to the Jeans length L_J . As shown in [10], all equilibria $\pm n$ with $n \geq 2$ are thermodynamically unstable (in the three micro-canonical, canonical and grand-canonical ensembles). They also exhibit a dynamical linear instability in the continuum limit where the motion follows the Vlasov equation, except for state $n = 2$ which becomes linearly stable very close to T_{c2} . Therefore, above T_{c1} the stable thermodynamical equilibrium of the discrete system (1) is the state $n = 0$ with $\rho = \bar{\rho}$ whereas below T_{c1} it is the state $n = 1$. However, as discussed in [8] quasi-stationary long-lived states can also exist and below T_{c2} we can expect the equilibrium $n = 2$ to be such a long-lived configuration.

As seen in [10], at low temperature ($\zeta_L \rightarrow \infty$) the density profile of the peak in the equilibrium $n = 1$ obeys:

$$\zeta \ll \frac{\ln \zeta_L}{\zeta_L} : \quad \frac{\rho_1(\zeta)}{\bar{\rho}} \simeq \frac{\zeta_L^2}{2 \cosh^2(\zeta_L/2)}, \quad (14)$$

whereas the density minimum at $x = L$ scales as:

$$\rho_1(\zeta_L) \sim \bar{\rho} e^{-\zeta_L^2/2} = \bar{\rho} e^{-\pi^2 T_{c1}/2T}. \quad (15)$$

For other states $\pm n$ we can obtain the asymptotics from (12). Note that the minimum energy which can be achieved by the OSC system is $E_{\min}(1) = -gM^2L/2$ when all particles are at rest at the same boundary, either $x = 0$ or $x = L$. It can only be reached by the equilibrium $n = \pm 1$ at zero temperature whereas other equilibria $\pm n$ with $n \geq 2$ have energies above $E_{\min}(n=2) = -gM^2L/4$.

C. Numerical simulations

From Eq.(1) we obtain the equations of motion of the N particles as:

$$\ddot{x}_i - 2g\bar{\rho}x_i = g\bar{\rho}L \left(\frac{N_i^+ - N_i^-}{N} - 1 \right), \quad (16)$$

where N_i^+ (resp. N_i^-) is the number of particles located to the right (resp. to the left) of particle i , that is with $x > x_i$. In practice, following [14, 15] we rank the particles in increasing order of x_i and when two particles “collide” we exchange their velocities so that the ordering remains valid at all times: $x_i \leq x_{i+1}$. Therefore, the numbers of particles to the left and to the right of particle i are constant: $N_i^- = i - 1$ and $N_i^+ = N - i$. Thus between two collisions the dynamics of particle i is given by:

$$\begin{aligned} x_i(t) = & x_i^{\text{eq}} + (x_i^0 - x_i^{\text{eq}}) \cosh \left(\frac{t - t_i^0}{t_{\text{dyn}}} \right) \\ & + v_i^0 t_{\text{dyn}} \sinh \left(\frac{t - t_i^0}{t_{\text{dyn}}} \right), \end{aligned} \quad (17)$$

where we defined x_i^{eq} as the (unstable) equilibrium position of particle i and t_{dyn} the typical dynamical time (for the homogeneous configuration):

$$x_i^{\text{eq}} = \frac{2i - 1}{2N} L \quad \text{and} \quad t_{\text{dyn}} = \frac{1}{\sqrt{2g\bar{\rho}}}. \quad (18)$$

In Eq.(17) x_i^0 and v_i^0 are the particle coordinate and velocity at time t_i^0 (which is taken as the time of the last collision). We use the event-driven scheme of [14] to follow the dynamics of the system. We store the position and velocity (x_i^0, v_i^0) of all particles as well as the time t_i^0 of their last collision (initially we set $t_i^0 = 0$). Then, we compute the collision time of each particle with its neighbours and we store the results in a heap structure, so that the next collision is at the root of this heap. Next, we advance to this first crossing by evolving the two colliding particles with Eq.(17), exchanging their velocities at collision and updating their last collision time t_i^0 . Finally, we compute the new three collision times associated with these two particles and their neighbours which we store in the heap. At next step we take care of the next collision. Therefore, we advance from one collision to the next and at each crossing we only need to update the trajectories of the colliding particles and their next crossing times. The collision time between particles i and $i + 1$ can be obtained analytically from Eq.(17). Indeed, this yields for the distance between neighbours an expression of the form $x_{i+1} - x_i = A + B e^{t/t_{\text{dyn}}} + C e^{-t/t_{\text{dyn}}}$ where A, B and C are constants. Then the condition $x_{i+1} = x_i$ leads to a quadratic equation for the variable $y = e^{t/t_{\text{dyn}}}$ which is easily solved. Therefore, both the trajectories and the collision times are computed “exactly” from analytical formulae. Their accuracy only depends on the numerical

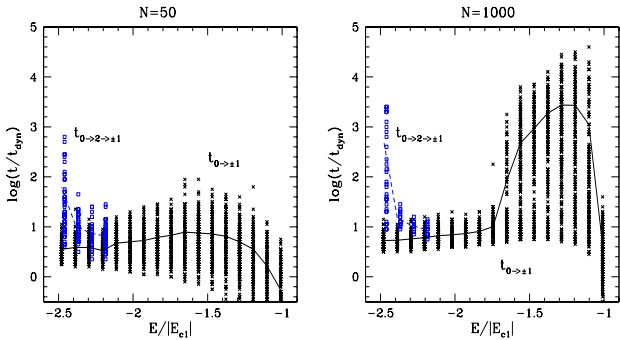


FIG. 1: The transition time $t_{0 \rightarrow \pm 1}$ from the unstable homogeneous state $n = 0$ to the stable equilibria $n = \pm 1$ as a function of total energy E , below the critical energy E_{c1} . At each energy the crosses are the numerical results obtained for 200 realizations of the initial condition $n = 0$, for a system of $N = 50$ (left panel) and $N = 1000$ particles (right panel). The solid line is the mean transition time obtained by averaging over these numerical results. The squares which are slightly shifted to the right show the transition times to states $n = \pm 1$ for realizations which happen to first relax to state $n = 2$ over a few dynamical times. The dashed curve is the average obtained for these systems.

accuracy of the computer and does not involve a discretization procedure to compute integrals or differential equations.

III. RELAXATION TO THERMODYNAMICAL EQUILIBRIUM

A. Homogeneous initial state $n = 0$

We study in this section the dynamics of the discrete OSC model (1) starting from initial conditions defined by the homogeneous thermodynamical equilibrium $n = 0$, i.e. Eq.(7) with $\rho = \bar{\rho}$. At high energies $E > E_{c1}$ the equilibrium $n = 0$ is stable (and there are no other thermodynamical equilibria) and we checked numerically that the system remains in this configuration. Therefore, we focus here on systems with total energies E below the critical energy E_{c1} where state $n = 0$ turns unstable (both for the thermodynamical analysis and the mean-field Vlasov dynamics) and two new stable equilibria $n = \pm 1$ appear, characterized by a density peak at $x = 0$ ($n = 1$) or at $x = L$ ($n = -1$). States ± 1 are symmetric with respect to $x = L/2$ and are essentially the same configuration. Hence we study here the relaxation of the OSC system from the homogeneous state $n = 0$ to the thermodynamical equilibria ± 1 .

1. Transition times

We first investigate the dependence on the energy E and on the number of particles N of the transition time $t_{0 \rightarrow \pm 1}$ from state $n = 0$ to either state $n = \pm 1$. Here we simply define the transition as the first time where $|K - K_1| < |K - K_0|$ and $|\bar{\Phi} - \bar{\Phi}_1| < |\bar{\Phi} - \bar{\Phi}_0|$ (i.e. the kinetic and self-gravity energies are closer to the levels of states $n = \pm 1$ than those of state $n = 0$). Thus, we display in Fig. 1 for several values of the total energy E the transition times $t_{0 \rightarrow \pm 1}$ obtained for 200 realizations (crosses) of the initial condition $n = 0$. Left (resp. right) panel corresponds to systems of $N = 50$ (resp. $N = 1000$) particles. The solid line is a mere average of these numerical results.

We can distinguish three regimes in Fig. 1. First, at low energies below $-1.7|E_{c1}|$ the transition proceeds over a few dynamical times (crosses and solid line). Moreover, the comparison of both panels shows that this time-scale does not display a significant dependence on the number of particles. Indeed, it is set by the mean-field dynamical instability growth rate associated with the fact that the homogeneous equilibrium $n = 0$ is linearly unstable for the Vlasov dynamics.

Second, at high energies above $-1.7|E_{c1}|$, closer to the critical energy E_{c1} , we find that transition times $t_{0 \rightarrow \pm 1}$ as defined above can be quite large and increase with the number of particles. We can also note that they show a very broad dispersion for different random realizations.

Third, at low energies below $E_{c2} \simeq -2.2|E_{c1}|$ we note that for some realizations of the homogeneous initial state the system does not directly relax to the equilibria $n = \pm 1$. It first exhibits a transition to the equilibrium $n = 2$ (which appears below the second critical energy E_{c2}) over a few t_{dyn} and remains trapped in this two-peak configuration over a long time-scale until it eventually evolves to a one-peak state $n = \pm 1$. This leads to the very long transition times labeled $t_{0 \rightarrow 2 \rightarrow \pm 1}$ shown by the squares in Fig. 1 (and the dotted curve for their average).

We shall discuss these three regimes in more details below.

2. Dynamical relaxation to $n = \pm 1$

We first consider a typical configuration of the first regime which exhibits a relaxation to equilibrium ± 1 driven by the collective dynamical instability. Thus we choose a particular realization with $N = 1000$ particles of the initial condition defined by the unstable equilibrium $n = 0$ at $E = -2|E_{c1}|$. We show in left panel of Fig. 2 the evolution of the various contributions (5)-(6) to the total energy E . The fluctuating curves are the gravitational self-energy $\bar{\Phi}$, the kinetic energy K and the external potential energy \bar{V} of the N -body system (from top down to bottom). The constant curve labeled E is its total energy which is conserved as we can check in the Figure. The other constant curves show the mean-field

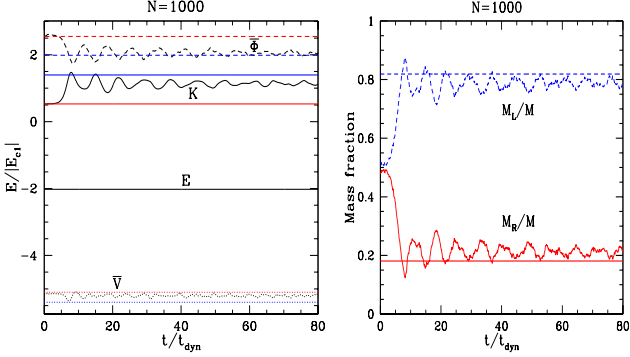


FIG. 2: *Left panel:* The evolution with time t of the various contributions K , $\bar{\Phi}$ and \bar{V} to the total energy E of a system of $N = 1000$ particles. We display the curves obtained for a particular realization of the initial condition defined by the unstable equilibrium $n = 0$ at energy $E = -2|E_{c1}|$. The constant curves are the mean-field energy levels of K (solid lines), $\bar{\Phi}$ (dashed lines) and \bar{V} (dotted lines) for the equilibria $n = 0$ and $n = \pm 1$. The system starts at levels $n = 0$ at $t = 0$ and undergoes a transition to levels $n = 1$ at $t \simeq 7t_{dyn}$. *Right panel:* The evolution with time of the masses M_L (dashed lines) and M_R (solid lines) located in the left and right parts of the system ($x < L/2$ and $x > L/2$). The constant lines show the values M_L, M_R of equilibrium $n = 1$.

energy levels of K , $\bar{\Phi}$ and \bar{V} for the equilibria $n = 0$ and $n = \pm 1$. Thus, we can see that the system starts at levels $n = 0$ and displays a transition to levels $n = \pm 1$ over a few dynamical times t_{dyn} . The fact that the transition time-scale is of order of a few t_{dyn} and does not depend on the number of particles, as was checked in Fig. 1 for $E < -1.7|E_{c1}|$, translates the fact that this is a collective instability. Indeed, as shown in [10] the thermodynamical equilibrium $n = 0$ becomes linearly unstable below the critical energy E_{c1} for the mean-field Vlasov dynamics. The growth rate of this instability saturates to $e^{t/t_{dyn}}$ at low energies [10] which sets the time-scale for the transition to equilibrium $n = \pm 1$. The right panel in Fig. 2 shows the evolution of the masses M_L and M_R located in the left and right parts of the system. It also clearly shows the dynamical instability which amplifies the small initial random imbalance $M_L - M_R$ to build a left-peak state after a few t_{dyn} . We can note that the relaxation is not fully complete as the system still exhibits some mean deviation and oscillations from the levels $n = 1$ for K and \bar{V} (and for masses M_L and M_R), although the largest energy component $\bar{\Phi}$ relaxes to its equilibrium level after $\sim 60t_{dyn}$. We found that these small departures persist up to 10^4t_{dyn} .

We present in Fig. 3 two snapshots of the density distribution for the realization used in Fig. 2, at times $t = 8$ and $12t_{dyn}$. We can see that the matter distribution has indeed evolved from the homogeneous state to a one-peak configuration close to equilibrium $n = 1$ at $t = 8t_{dyn}$. However, it has not yet fully relaxed and some collective oscillations persist as already seen in Fig. 2, which also

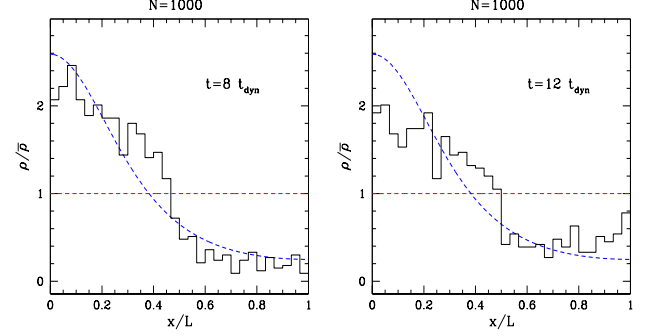


FIG. 3: Two snapshots of the density distribution $\rho(x)$ at times $t = 8$ and $12t_{dyn}$. The histogram shows the matter distribution of the N -body system over 30 bins. The dashed curves are equilibria $n = 0$ (constant density) and $n = 1$ (peak at $x = 0$).

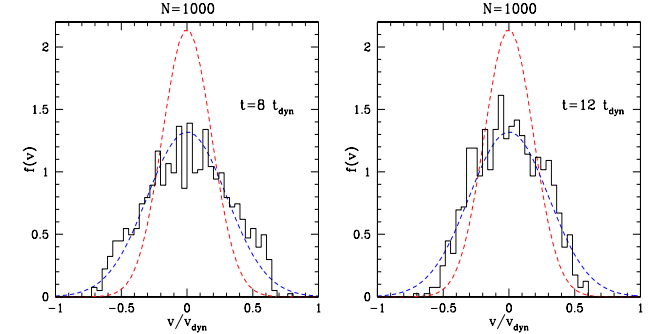


FIG. 4: Two snapshots of the velocity distribution $f(v)$ at times $t = 8$ and $12t_{dyn}$, in units of v/v_{dyn} where we defined $v_{dyn} = L/t_{dyn}$. The histogram corresponds to the N -body system whereas the dashed curves are equilibria $n = 0$ (narrow Gaussian) and $n = 1$ (broad Gaussian).

lead to oscillations of the density and width of the peak.

We show in Fig. 4 two snapshots of the velocity distribution at the same times $t = 8$ and $12t_{dyn}$. It has again evolved from the distribution $n = 0$ to the distribution $n = 1$ at time $t = 8t_{dyn}$. Although there are some oscillations in the tails (as seen from the right panel at time $12t_{dyn}$ and the fluctuations of K in Fig. 2) we can see that the relaxation of the velocity distribution is rather efficient and always remains close to the equilibrium $n = 1$.

We checked that for a small number of particles $N = 50$ the behaviour of the system is the same in this energy range. The states $n = \pm 1$ and $n = 0$ are well separated and the system exhibits a transition to equilibrium ± 1 over a few dynamical times.

3. Close to the critical energy E_{c1}

We now investigate the evolution of systems at higher energies $E > -1.7|E_{c1}|$, closer to the critical energy E_{c1} .

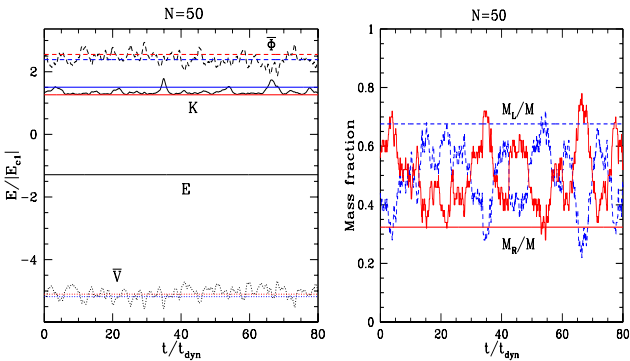


FIG. 5: The evolution of the energy components K , $\bar{\Phi}$, \bar{V} and E (left panel) and of the masses M_L , M_R (right panel) as in Fig. 2. We show the curves obtained for a particular realization with $N = 50$ particles of the initial homogeneous state at $E = -1.3|E_{c1}|$. The system keeps wandering over states $n = 0, \pm 1$ and does not settle into a stable equilibrium.

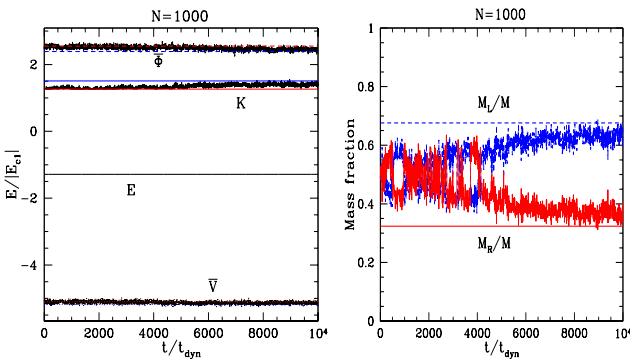


FIG. 6: The evolution of the energy components K , $\bar{\Phi}$, \bar{V} and E (left panel) and of the masses M_L , M_R (right panel) as in Fig. 2. We show the curves obtained for a particular realization with $N = 1000$ particles of the initial homogeneous state at $E = -1.3|E_{c1}|$ which only relaxes to equilibrium $n = 1$ over $\sim 8000t_{\text{dyn}}$.

We first display in Fig. 5 the evolution of the energy and mass components for a system of $N = 50$ particles at energy $E = -1.3|E_{c1}|$. The right panel shows that the system evolves over a time scale set by the dynamical time t_{dyn} , in agreement with Fig. 1, but it does not settle into a stable equilibrium. Indeed, it keeps fluctuating indefinitely from left-peak to right-peak configurations and wanders over states $n = 0, \pm 1$, as can also be seen from the fluctuating energy levels in left panel of Fig. 5 (we checked numerically that this fluctuating behaviour remains unchanged at least up to 10^4t_{dyn}). Therefore, in this regime the transition time $t_{0 \rightarrow \pm 1}$ which was shown in Fig. 1 merely corresponds to the first time where the system gets close to a state characterized by a density peak close to a boundary, as equilibria ± 1 , but the fluctuations are too large to let the system settle down in such

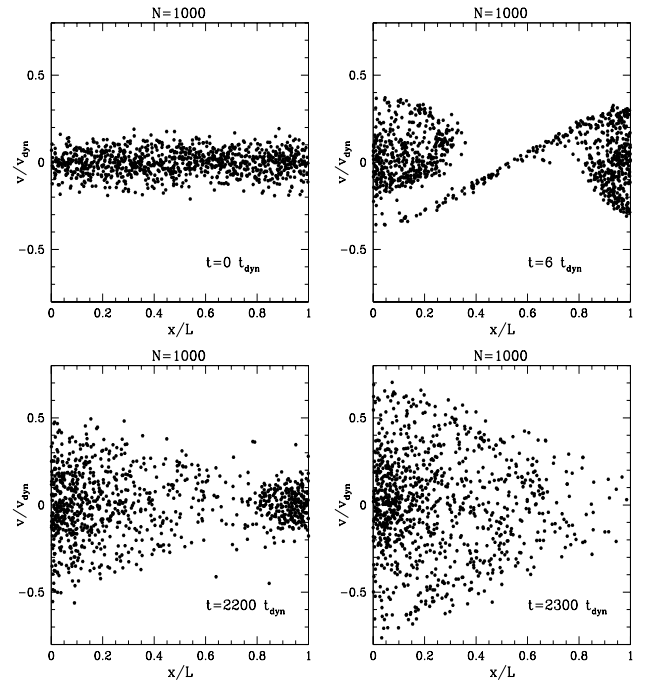


FIG. 7: Four snapshots of the phase-space distribution $f(x, v)$ at times $t = 0, 6, 2200$ and $2300t_{\text{dyn}}$ for a system of $N = 1000$ particles. For this particular realization of the initial homogeneous state $n = 0$ the system first undergoes a transition to the equilibrium $n = 2$ over $6t_{\text{dyn}}$ and only relaxes to the one-peak state $n = 1$ at $t \sim 2250t_{\text{dyn}}$.

a stable configuration. Hence it keeps exploring various states with both left or right overdensities.

Next, we show in Fig. 6 the evolution of a system of $N = 1000$ particles with the same energy $E = -1.3|E_{c1}|$. Because of the larger number of particles the system starts with a more balanced state $(M_L - M_R)/M \sim 1/\sqrt{N}$ and the fluctuations with time of various quantities are smaller. Therefore, we find that the system again wanders for a long time over states with $M_L \sim M_R$ and even exhibits several oscillations from left-peak to right peak configurations but it now manages to eventually settle down into a stable equilibrium $n = \pm 1$ after $\sim 8000t_{\text{dyn}}$. Indeed, as the system starts close to $M_L = M_R$ small fluctuations are initially sufficient to evolve from $M_L > M_R$ to $M_L < M_R$ but once it has converged close to either one of equilibria ± 1 the fluctuations are no longer sufficient to escape to the symmetric state.

4. Below the second critical energy E_{c2}

Finally, we noticed in Fig. 1 that at low energies below E_{c2} there are cases where the system does not exhibit a direct transition to stable equilibria ± 1 . It first evolves to the two-peak equilibrium $n = 2$ over a few dynamical

times and next relaxes to the stable equilibrium $n = \pm 1$ over a much longer time-scale. We show in Fig. 7 four snapshots of the phase-space distribution $f(x, v)$ for such a realization at $E = -2.5|E_{c1}|$, with $N = 1000$ particles, which first relaxes to state $n = 2$. Thus, we can see that the system has already evolved from an homogeneous configuration to a two-peak state at $t = 6t_{\text{dyn}}$. It remains in such a configuration until $\sim 2250t_{\text{dyn}}$ while particles slowly diffuse out of the right density peak and at $t = 2300t_{\text{dyn}}$ it has relaxed to the stable equilibrium $n = 1$. Of course the energy levels show the same transitions from $n = 0$ to $n = 2$ and finally to $n = 1$. In agreement with the calorific curve shown in Fig. 4 of [10] we note that for a fixed total energy E the temperature grows (the velocity distribution becomes broader) as we go from state $n = 0$ to $n = 2$ and finally to $n = 1$. We shall investigate in more details the transition from equilibrium $n = 2$ to state $n = 1$ in sect. III B below. For systems with $N = 50$ particles we found that 58 out of 200 realizations exhibit this two-stage behaviour at $E = -2.5|E_{c1}|$ whereas for $N = 1000$ particles this only occurs for 30 out of 200 realizations. Indeed, as seen in [10] the linear growth rate of the two-peak instability obtained for the mean-field Vlasov dynamics is smaller than the growth rate associated with a one-peak perturbation (higher wavenumbers are less unstable thanks to the finite temperature, following the usual Jeans instability). Therefore, systems with a larger number of particles which follow more closely the mean-field dynamics should more frequently evolve directly towards a one-peak state.

B. Initial equilibrium $n = 2$

We now study in this section the relaxation to the stable equilibrium $n = \pm 1$ starting from the equilibrium $n = 2$.

1. Transition times

We first show in Fig. 8 the transition times $t_{2 \rightarrow \pm 1}$ obtained for various realizations of the initial equilibrium $n = 2$, as a function of total energy, for systems with $N = 50$ (left panel) and $N = 500$ particles (right panel). We also plot the mean transition times derived from these realizations (solid line) and the theoretical prediction (dashed-line) of eq.(63). As in sect. III A 1 we defined the transition as the first time where $|K - K_1| < |K - K_2|$ and $|\bar{\Phi} - \bar{\Phi}_1| < |\bar{\Phi} - \bar{\Phi}_2|$ (i.e. the kinetic and self-gravity energies are closer to the levels of states $n = \pm 1$ than those of state $n = 2$). We can see that there is a large dispersion from one realization to another for small systems ($N = 50$) but the mean transition time agrees reasonably well with Eq.(63). For larger N where discrete effects are less violent ($N = 500$) the dispersion is much smaller and we recover the theoretical prediction (63) which is derived in the limit of large N (which allows a pertur-

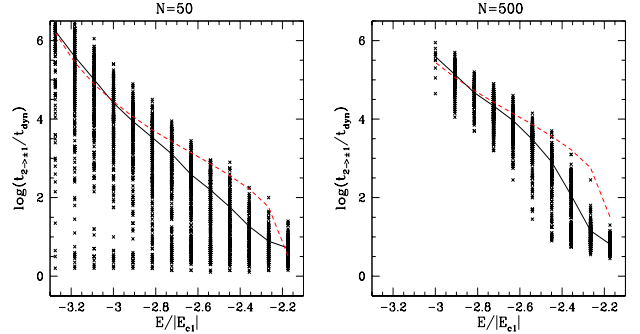


FIG. 8: The transition time $t_{2 \rightarrow \pm 1}$ from the two-peak equilibrium $n = 2$ to the one-peak stable equilibria $n = \pm 1$ as a function of total energy E . The crosses correspond to various realizations of the initial equilibrium $n = 2$ at a given energy, for systems of $N = 50$ (left panel) and $N = 500$ particles (right panel). The solid line is the mean transition time obtained from these realizations whereas the dashed-line is the theoretical prediction (63).

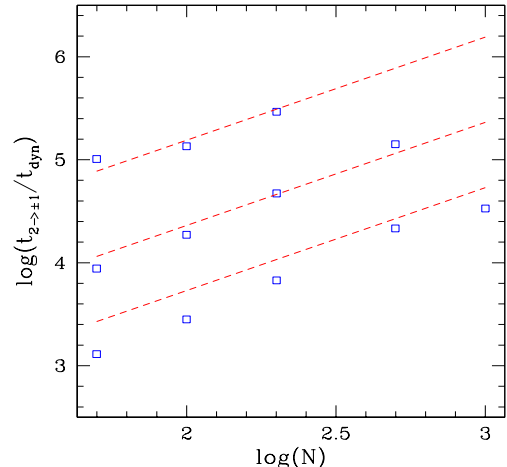


FIG. 9: The mean transition time $t_{2 \rightarrow \pm 1}$ as a function of the number N of particles. The various lines correspond to total energies $E = -2.73|E_{c1}|$, $-2.9|E_{c1}|$ and $-3.1|E_{c1}|$ from bottom to top. The squares are the numerical results (averaged over many realizations, solid line in Fig. 8) whereas the dashed-lines are the theoretical prediction (63) (as in Fig. 8).

bative analysis). In particular, note the steep increase at low energies when the two narrow density peaks are separated by an almost void region and there is a very slow diffusion of particles out of the smallest peak until the system reaches the abrupt transition point discussed below in Fig. 10 where a collective instability merges the smallest peak into the largest one. We further discuss the dependence on energy of $t_{2 \rightarrow \pm 1}$ in Sect. III B 3 below where we detail the theoretical calculation of the transition time.

Next, we present in Fig. 9 the mean transition time

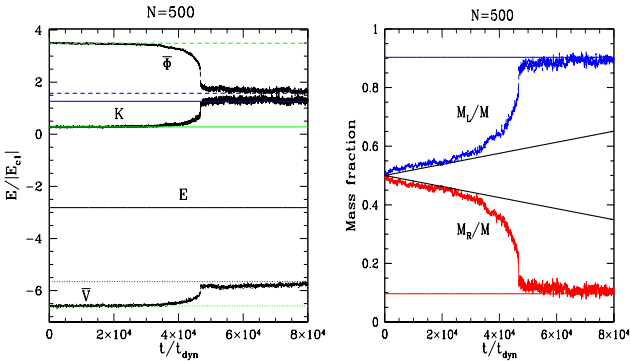


FIG. 10: *Left panel:* The evolution with time t of the various contributions K , $\bar{\Phi}$ and \bar{V} to the total energy E of a system of $N = 500$ particles. We display the curves obtained for a particular realization of the initial condition defined by the unstable equilibrium $n = 2$ at energy $E = -2.8|E_{cl}|$. The constant curves are the mean-field energy levels of K (solid lines), $\bar{\Phi}$ (dashed lines) and \bar{V} (dotted lines) for the equilibria $n = 1$ and $n = 2$. The system undergoes a transition from levels $n = 2$ to levels $n = 1$ at $t \sim 4.7 \times 10^4 t_{dyn}$. *Right panel:* The evolution with time of the masses M_L (dashed lines) and M_R (solid lines) located in the left and right parts of the system ($x < L/2$ and $x > L/2$). The constant lines show the values M_L, M_R of equilibrium $n = 1$. The two linear solid lines starting from $M_L = M_R = M/2$ at $t = 0$ are the theoretical estimate (62) for the mass transfer between both density peaks.

$t_{2 \rightarrow \pm 1}$ as a function of the number of particles N , for various total energies. We compare the numerical results (squares) with the theoretical predictions (dashed lines) of Eq.(63). We can check that the agreement is reasonably good and that the transition time scales linearly as N . In the limit $N \rightarrow \infty$ the equilibrium $n = 2$ becomes stable, in agreement with the mean-field analysis of [10] where it was shown that this state is linearly stable for the Vlasov dynamics.

2. Diffusive relaxation to $n = \pm 1$

We first show in Fig. 10 the evolution of the various contributions to the total energy, for a particular realization with $N = 500$ particles of the initial condition defined by the unstable equilibrium $n = 2$ at energy $E = -2.8|E_{cl}|$. We can see that the system displays a transition from levels $n = 2$ to levels $n = 1$ at $t \sim 4.7 \times 10^4 t_{dyn}$. We can note that there is first a slow drift up to $\sim 4.7 \times 10^4 t_{dyn}$ where there is a sudden transition towards energy levels of $n = 1$. This is more clearly seen in the right panel which displays the evolution of the masses located to the left (M_L at $x < L/2$) and to the right (M_R at $x > L/2$) of the system. We can see that there is a slow transfer of matter from the right peak to the left peak until $\sim 4.7 \times 10^4 t_{dyn}$. Then, there is a sudden jump where the mass ratio reaches its equilib-

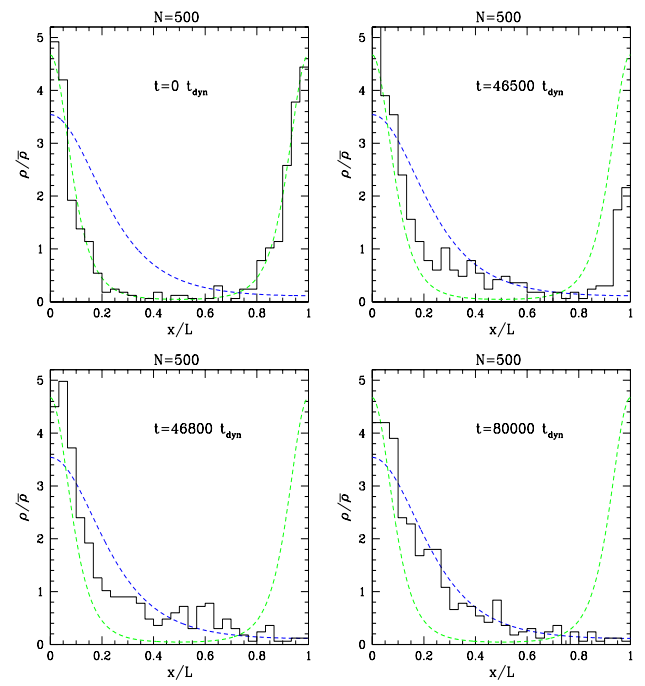


FIG. 11: Four snapshots of the density distribution $\rho(x)$ at times $t = 0, 46500, 46800$ and $80000 t_{dyn}$. The histogram shows the matter distribution of the N -body system over 30 bins. The dashed curves are equilibria $n = 1$ and $n = 2$.

rium value after a few dynamical times. This suggests that there is first a slow evolution over a few thousand t_{dyn} with a quasi-static exchange of matter between both density peaks which remain close to local thermodynamical equilibrium states for separate clouds until the ratio of both peak masses becomes so large that the system turns dynamically unstable and relaxes towards equilibrium $n = 1$ over a few dynamical times t_{dyn} . Indeed, as shown in [10] both statistical equilibria $n = 1$ and $n = 2$ are stable at low temperature for the mean-field Vlasov dynamics (although only state $n = 1$ is thermodynamically stable). By continuity, this means that there is a threshold where the system leaves the basin of attraction of two-peaks configurations to enter the basin of attraction of the one-peak equilibrium. Indeed, two-peak states close to the equilibrium $n = 2$ (i.e. with a mass ratio of both clouds close to unity) have negative stability eigenvalues and remain stable with respect to the mean-field Vlasov dynamics. On the other hand, two-peak states with a high mass ratio can be seen as small perturbations of the one-peak equilibrium $n = 1$ which is itself stable. Therefore, such two-peak states undergo a collective instability which leads to relaxation towards the stable equilibrium $n = 1$. For the system shown in Fig. 10 this transition between two different stability regions of the mean-field dynamics occurs at $t \sim 4.7 \times 10^4 t_{dyn}$.

The solid lines starting from $M_L = M_R = M/2$ at $t = 0$ are the theoretical estimate (62) which has been

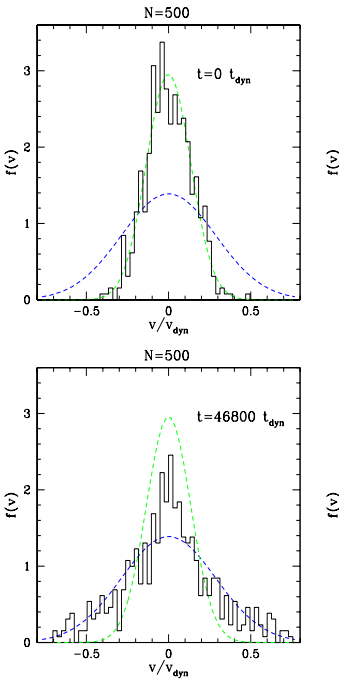


FIG. 12: Four snapshots of the velocity distribution $f(v)$ at times $t = 0, 46500, 46800$ and $80000t_{dyn}$. The histogram corresponds to the N –body system whereas the dashed curves are equilibria $n = 2$ (narrow Gaussian) and $n = 1$ (broad Gaussian).

normalized by a factor 0.2 of order unity to match the slope at early times of the mass transfer. This was then used to predict the transition times shown in Figs. 8-9 for a broad range of total energies and particle numbers.

We present in Fig. 11 four snapshots of the density distribution $\rho(x)$ for the N –body system as compared with the mean-field equilibria $n = 1$ and $n = 2$. In agreement with Fig. 10 we recover the sudden transition at $\sim 47000t_{dyn}$ from a two-peak state to a one-peak state, after the right peak has slowly lost about half its mass to the left peak. We can also check that the density distribution relaxes to the statistical equilibrium $n = 1$.

In a similar fashion, we show in Fig. 12 the velocity distribution $f(v)$, which is also seen to relax from the equilibrium $n = 2$ to state $n = 1$. We note that the relaxation of the velocity distribution seems to be more efficient than for the density distribution. Indeed, at $t = 46500t_{dyn}$ it is still close to the Gaussian $n = 2$ whereas at $t = 46800t_{dyn}$ it is already close to the Gaussian $n = 1$.

Finally, we display in Fig. 13 four snapshots of the phase-space distribution $f(x, v)$. It shows again that the transition from $n = 2$ to $n = 1$ proceeds in two steps, with a slow diffusion followed by a sudden disruption of the smallest density peak. In particular, we can see in the upper right panel of Fig. 13 that the right peak still exists as a distinct object at $t = 46500t_{dyn}$ and has disappeared by $t = 46800t_{dyn}$.

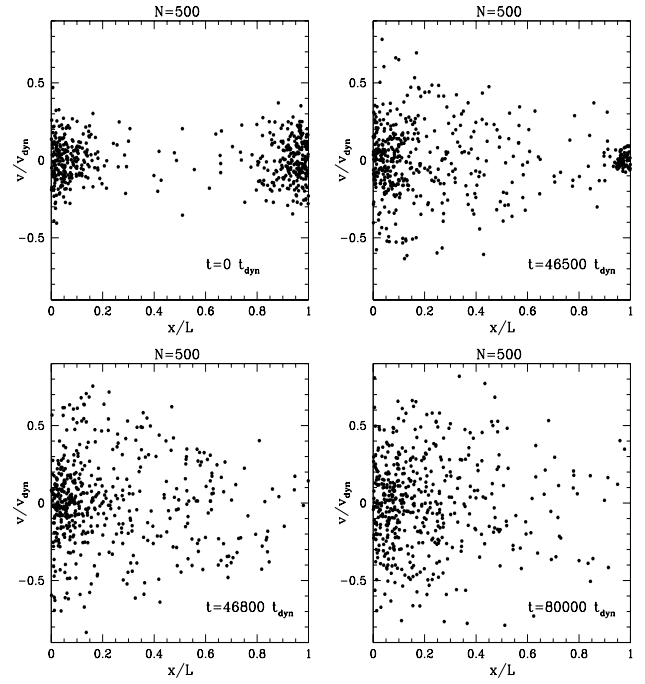


FIG. 13: Four snapshots of the phase-space distribution $f(x, v)$ at times $t = 0, 46500, 46800$ and $80000t_{dyn}$.

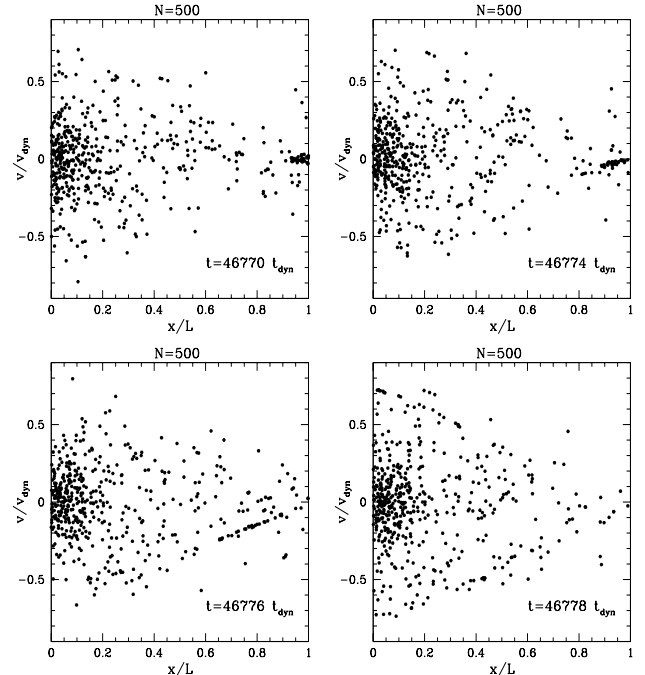


FIG. 14: Four snapshots of the phase-space distribution $f(x, v)$ at times $t = 46770, 46774, 46776$ and $46778t_{dyn}$ around the transition to the one-peak state.

We show in Fig. 14 four snapshots of the phase-space distribution around the transition to the one-peak state. We can see that what is left of the right peak at $t \sim 46770t_{\text{dyn}}$ exhibits a strong deformation at $46774t_{\text{dyn}}$ and is absorbed into the left peak at $46776t_{\text{dyn}}$. This details the second step of the transition as a collective dynamic instability which merges the remains of the smallest peak into the largest one over a few dynamical times t_{dyn} .

3. Estimate of the mean transition time $t_{2 \rightarrow \pm 1}$

We describe in this section how the mean transition times $t_{2 \rightarrow \pm 1}$ shown in Figs. 8-9 can be estimated by analytical means.

The relaxation towards thermal equilibrium of N -body systems such as the OSC model is often studied through the stochastic dynamics of a test particle in interaction with the rest of the system, as described by a Fokker-Planck equation [16]. In such cases, the test particle experiences both a systematic drift (such as the dynamical friction suffered by a high-velocity star moving through a cloud of low-velocity stars [17, 18]) and a diffusion, due to random encounters, which both grow linearly with time. Moreover, if the correlation times are small one can use a Markovian approximation so that the relaxation of the test particle in the thermal bath is described by a Fokker-Planck equation [16], which is fully parameterized by the friction and diffusion coefficients. One may then describe for instance the relaxation of the velocity distribution of the test particle and its approach to thermal equilibrium [19, 20].

In the case we consider here, the system starts in an inhomogeneous mean-field equilibrium with two peaks at the boundaries. Then, we model the slow loss of matter of the smallest peak, displayed in Fig. 10, as a diffusive process which makes particles located in the smallest potential well escape to the other potential well. Since the escape time is shorter for the smaller potential well we neglect the flux from particles moving from the deepest well to the smallest one. This is consistent with right panel of Fig. 10 which shows that the lightest peak is almost steadily losing mass. Here we shall neglect the evolution with time of the small density peak due to mass loss and we simply consider the bistable system $n = 2$ made of the symmetric double potential well $\phi(x)$ which has two minima at the walls $x = 0, L$ and a maximum at $x = L/2$. Then, we focus on the behaviour of a test mass m orbiting in the left peak and we study the evolution of its energy ϵ (whence of its orbit) due to encounters with other discrete particles. Computing the associated friction and diffusion coefficients we obtain the average time τ required to reach the barrier energy $\phi(L/2) - \phi(0)$ and escape from the potential well through a Fokker-Planck dynamics. This allows us to estimate the transition time $t_{2 \rightarrow \pm 1} \sim \tau$ to relax to the thermodynamically stable equilibrium $n = 1$.

In order to separate the mean-field dynamics from the

discrete effects which give rise to the diffusion of particles we write the Hamiltonian (1) as:

$$\mathcal{H}_N = m(\mathcal{H}_0 + \mathcal{H}_I) \quad (19)$$

where we factorized the mass m which plays no role and we defined the mean-field Hamiltonian \mathcal{H}_0 by:

$$\mathcal{H}_0 = \sum_{j=1}^N \left[\frac{v_j^2}{2} + \Phi_0(x_j) + V(x_j) \right] \quad (20)$$

and the interaction Hamiltonian \mathcal{H}_I by:

$$\mathcal{H}_I = e^{\omega t} \left[gm \sum_{j>j'} |x_j - x_{j'}| - \sum_j \Phi_0(x_j) \right]. \quad (21)$$

In Eq.(20) the mean-field gravitational potential Φ_0 is given by Eq.(3) where $\rho(x')$ is the mean-field equilibrium distribution (7). In Eq.(21) we added a factor $e^{\omega t}$ for the computation of perturbative eigenmodes and we shall consider the limit $\omega \rightarrow 0^+$. Thus, \mathcal{H}_0 describes the mean-field dynamics whereas \mathcal{H}_I describes the discrete effects which vanish in the limit $N \rightarrow \infty$. Therefore, we consider \mathcal{H}_I as a perturbation to \mathcal{H}_0 and we apply a perturbative analysis to the dynamics of individual particles. Here it is convenient to work with the action-angle variables (J, w) defined from the Hamiltonian \mathcal{H}_0 which describe the motion of a particle of energy $\epsilon = v^2/2 + \phi_0$ along its non-perturbed orbit in the equilibrium potential $\phi_0 = \Phi_0 + V$ from position x_- to x_+ [18, 21]:

$$J = \frac{2}{2\pi} \int_{x_-}^{x_+} dx \sqrt{2(\epsilon - \phi_0(x))}, \quad (22)$$

and:

$$w = \Omega \int_{x_-}^x \frac{dx'}{\sqrt{2(\epsilon - \phi_0(x'))}} \quad \text{with} \quad \Omega = \frac{d\epsilon}{dJ}. \quad (23)$$

Thus, $\mathcal{H}_0 = \mathcal{H}_0(J_j)$ only depends on the actions J_j . On the other hand, thanks to the periodicity of 2π with respect to w of the non-perturbed orbits $x(J, w)$ we can write the two-body interaction as:

$$gm|x - x'| = \sum_{k, k'=-\infty}^{\infty} \phi_{k, k'}(J, J') e^{i(kw - k'w')}, \quad (24)$$

which defines the Fourier coefficients $\phi_{k, k'}(J, J')$. Besides, from Eq.(3) the mean-field potential $\Phi_0(x)$ reads:

$$\Phi_0(x) = g \int dJ' dw' f_0(J') |x - x'| \quad (25)$$

$$= \frac{2\pi}{m} \sum_{k=-\infty}^{\infty} \int dJ' f_0(J') \phi_{k, 0}(J, J') e^{ikw}, \quad (26)$$

where we used the canonical change of variable $dx dw = dJ dw$ and f_0 is the mean-field equilibrium distribution

(7). This yields:

$$\begin{aligned} \mathcal{H}_I = & e^{\omega t} \left[\frac{1}{2} \sum_{j,j'} \sum_{k,k'} \phi_{k,k'}(J, J') e^{i(kw - k'w')} \right. \\ & \left. - \frac{2\pi}{m} \sum_j \sum_k \int dJ' f_0(J') \phi_{k,0}(J, J') e^{ikw} \right] \end{aligned} \quad (27)$$

Then, the equations of motion read:

$$\dot{J}_j = -\frac{\partial}{\partial w}(\mathcal{H}_0 + \mathcal{H}_I), \quad \dot{w}_j = \frac{\partial}{\partial J}(\mathcal{H}_0 + \mathcal{H}_I). \quad (28)$$

We write the action-angle trajectories $\{J(t), w(t)\}$ as the perturbative expansions $J = J^{(0)} + J^{(1)} + J^{(2)} + \dots$ where $J^{(k)}$ is formally of order k over \mathcal{H}_I . At zeroth-order we simply have:

$$\dot{J}_j^{(0)} = -\frac{\partial \mathcal{H}_0}{\partial w_j} = 0, \quad \dot{w}_j^{(0)} = \frac{\partial \mathcal{H}_0}{\partial J_j} = \Omega(J_j^{(0)}), \quad (29)$$

which yields the mean-field equilibrium orbits:

$$J_j^{(0)} = \text{constant} \quad \text{and} \quad w_j^{(0)} = w_j^{(0)}(0) + \Omega(J_j^{(0)})t. \quad (30)$$

At first order we obtain:

$$\dot{J}_j^{(1)} = -\frac{\partial \mathcal{H}_I}{\partial w_j}, \quad \dot{w}_j^{(1)} = \frac{d\Omega}{dJ} J_j^{(1)} + \frac{\partial \mathcal{H}_I}{\partial J_j}, \quad (31)$$

where we can substitute the zeroth-order orbits in the r.h.s. Using the property $\phi_{k',k}(J', J) = \phi_{k,k'}(J, J')^*$ obtained from Eq.(24) a simple calculation yields (e.g. [22]):

$$J_j^{(1)} = -\frac{\partial \chi}{\partial w_j}, \quad w_j^{(1)} = \frac{\partial \chi}{\partial J_j}, \quad (32)$$

with:

$$\begin{aligned} \chi = & e^{\omega t} \left[\frac{1}{2} \sum_{j,j'} \sum_{k,k'} \frac{\phi_{k,k'}}{\omega + i(k\Omega - k'\Omega')} e^{i(kw - k'w')} \right. \\ & \left. - \frac{2\pi}{m} \sum_j \sum_k \int dJ' f_0(J') \frac{\phi_{k,0}}{\omega + ik\Omega} e^{ikw} \right]. \end{aligned} \quad (33)$$

At second order we need to follow the first-order orbits in the r.h.s of Eq.(28) and we have for the actions:

$$\dot{J}_j^{(2)} = -\sum_{j'} \frac{\partial^2 \mathcal{H}_I}{\partial w_j \partial J_{j'}} J_{j'}^{(1)} - \sum_{j'} \frac{\partial^2 \mathcal{H}_I}{\partial w_j \partial w_{j'}} w_{j'}^{(1)}. \quad (34)$$

Using again $\phi_{k',k} = \phi_{-k,-k'} = \phi_{k,k'}^*$ and taking the average (with the equilibrium distribution $f_0(J)$) over the actions and angles $\{J^{(0)}, w^{(0)}(0)\}$ of other particles yields

at order $1/N$ (note that $\phi_{k,k'} \propto m$ and $m \propto 1/N$):

$$\begin{aligned} \langle \dot{J}^{(2)} \rangle = & e^{2\omega t} \frac{\partial}{\partial J} \left[\frac{2\pi}{m} \int dJ' f_0(J') \sum_{k,k'} \frac{\omega k^2 |\phi_{k,k'}|^2}{\omega^2 + (k\Omega - k'\Omega')^2} \right. \\ & \left. - \frac{4\pi^2}{Nm^2} \int dJ' dJ'' f_0(J') f_0(J'') \sum_k \frac{\omega k^2 \phi_{k,0} \phi_{k,0}^*}{\omega^2 + (k\Omega)^2} \right] \\ & - e^{2\omega t} \frac{2\pi}{m} \int dJ' f_0(J') \frac{\partial}{\partial J'} \sum_{k,k'} \frac{\omega k k' |\phi_{k,k'}|^2}{\omega^2 + (k\Omega - k'\Omega')^2} \end{aligned} \quad (35)$$

Then, using $\lim_{\omega \rightarrow 0^+} \omega/(\omega^2 + x^2) = \pi \delta_D(x)$ where δ_D is Dirac's distribution, the limit $\omega \rightarrow 0^+$ gives:

$$\begin{aligned} \langle \dot{J}^{(2)} \rangle = & \frac{2\pi^2}{m} \int dJ' f_0(J') \sum_{k,k'} \left(k \frac{\partial}{\partial J} - k' \frac{\partial}{\partial J'} \right) \\ & \times |\phi_{k,k'}|^2 k \delta_D(k\Omega - k'\Omega'), \end{aligned} \quad (36)$$

which does not depend on time. From these results we can obtain the mean drift and diffusion of the action J of a test particle. First, the average change $\langle \Delta J \rangle = \langle J(t_2) - J(t_1) \rangle$ of the action over a time-interval $\Delta t = t_2 - t_1$ reads at order $1/N$:

$$\langle \frac{\Delta J}{\Delta t} \rangle = \langle \frac{\Delta J^{(1)} + \Delta J^{(2)}}{\Delta t} \rangle = \langle \dot{J}^{(2)} \rangle \quad (37)$$

since $\langle \dot{J}^{(2)} \rangle$ is constant and $\langle J^{(1)} \rangle = 0$ when we average [22] over the angles $w^{(0)}(0)$ as seen from Eq.(32). Next, from Eqs.(32)-(33) the mean-square change $\langle (\Delta J)^2 \rangle$ reads at order $1/N$:

$$\begin{aligned} \langle (\Delta J)^2 \rangle = & e^{2\omega t_1} \frac{2\pi}{m} \int dJ' f_0(J') \sum_{k,k'} \frac{k^2 |\phi_{k,k'}|^2}{\omega^2 + (k\Omega - k'\Omega')^2} \\ & \times (1 + e^{2\omega \Delta t} - 2e^{\omega \Delta t} \cos[(k\Omega - k'\Omega')\Delta t]) \\ & - e^{2\omega t_1} \frac{4\pi^2}{Nm^2} \int dJ' dJ'' f_0(J') f_0(J'') \sum_k \frac{k^2 \phi_{k,0} \phi_{k,0}^*}{\omega^2 + (k\Omega)^2} \\ & \times (1 + e^{2\omega \Delta t} - 2e^{\omega \Delta t} \cos[k\Omega \Delta t]). \end{aligned} \quad (38)$$

The limit $\omega \rightarrow 0^+$ now gives:

$$\begin{aligned} \langle \frac{(\Delta J)^2}{\Delta t} \rangle = & \frac{2\pi}{m} \int dJ' f_0(J') \sum_{k,k'} 2k^2 |\phi_{k,k'}|^2 \\ & \times \frac{1 - \cos[(k\Omega - k'\Omega')\Delta t]}{\Delta t (k\Omega - k'\Omega')^2} \\ & - \frac{4\pi^2}{Nm^2} \int dJ' dJ'' f_0(J') f_0(J'') \sum_k 2k^2 \phi_{k,0} \phi_{k,0}^* \\ & \times \frac{1 - \cos[k\Omega \Delta t]}{\Delta t (k\Omega)^2}. \end{aligned} \quad (39)$$

As seen from Eqs.(32)-(33) the action J and angle w of each particle in a given realization (i.e. without performing any averaging) are modified by discrete effects over

a time-scale which grows as \sqrt{N} and as expected in the limit $N \rightarrow \infty$ we recover the mean-field dynamics. Since we consider the limit of large number of particles, which justifies the perturbative approach (19), let us consider in Eq.(39) time-scales of order $\Delta t \sim \sqrt{N} \rightarrow \infty$. Using the equality $\lim_{t \rightarrow \infty} (1 - \cos tx)/tx^2 = \pi\delta_D(x)$ we obtain in this large- N limit:

$$\langle \frac{(\Delta J)^2}{\Delta t} \rangle_\infty = \frac{4\pi^2}{m} \int dJ' f_0(J') \sum_{k,k'} k^2 |\phi_{k,k'}|^2 \delta_D(k\Omega - k'\Omega'). \quad (40)$$

Thus, both the mean drift and diffusion of the action occur through resonances between particle orbits (also [22]). Moreover, they both grow linearly with time. We can note that [23] also obtained a diffusion coefficient of the form (39) which decays as $1/t$ with an oscillatory behaviour for the HMF model in the limit of low temperatures where a density peak appears. However, [23] approximated the core orbits by an harmonic oscillator of unique frequency Ω_0 so that there was no integration over Ω' as in Eqs.(36),(39) through the dependence $\Omega'(J')$. In order to take the large-time or large- N limit it is necessary to take into account the distribution of orbital frequencies $f_0(\Omega)$. Note that our approach also applies to any Hamiltonian system with two-body interactions, such as the HMF model. At this point, it is convenient to change variable from the action J to the energy $\epsilon(J) = v^2/2 + \phi_0$ (both are defined from the mean-field Hamiltonian \mathcal{H}_0). Using the expansion:

$$\Delta\epsilon = \Omega\Delta J + \frac{1}{2} \frac{d\Omega}{dJ} (\Delta J)^2 + \dots \quad (41)$$

we obtain at order $1/N$:

$$\langle \frac{\Delta\epsilon}{\Delta t} \rangle = \frac{4\pi^2}{m} \int dJ' f_0(J') \sum_{k,k'=1}^{\infty} \left(k \frac{\partial}{\partial J} - k' \frac{\partial}{\partial J'} \right) \times |\phi_{k,k'}|^2 k\Omega \delta_D(k\Omega - k'\Omega'), \quad (42)$$

and:

$$\langle \frac{(\Delta\epsilon)^2}{\Delta t} \rangle = \frac{8\pi^2}{m} \int dJ' f_0(J') \sum_{k,k'=1}^{\infty} |\phi_{k,k'}|^2 k^2 \Omega^2 \delta_D(k\Omega - k'\Omega'). \quad (43)$$

In Eqs.(42)-(43) we changed the sums over k and k' from $]-\infty, \infty[$ to $[1, \infty[$ which gave a factor 2. We can check from Eq.(42) that the transfer of energy $\Delta\epsilon(J' \rightarrow J) = -\Delta\epsilon(J \rightarrow J')$ is anti-symmetric over (J, J') so that the mean change of energy over all particles (with the distribution $f_0(J)$) vanishes. This is related to the conservation of energy by the Hamiltonian dynamics. On the other hand $(\Delta\epsilon)^2$ is symmetric. We now focus on the low temperature regime $T \rightarrow 0, \zeta_L \rightarrow \infty$, where the initial state $n = 2$ consists of two narrow density peaks at the boundaries $x = 0, L$. Then, from the asymptotic behaviour (14) and the rescaling (12) we obtain for the properties of the core which contains most of the mass

the scalings:

$$\frac{\rho_c}{\bar{\rho}} \sim \zeta_L^2, \frac{R_c}{L} \sim \zeta_L^{-2}, \frac{\Omega_c}{\Omega_{\text{dyn}}} \sim \zeta_L, \frac{v_c}{v_{\text{dyn}}} \sim \zeta_L^{-1}, \frac{J_c}{J_{\text{dyn}}} \sim \zeta_L^{-3}, \quad (44)$$

where $\rho_c, R_c, \Omega_c, v_c$ and J_c are the typical density, orbital radius, frequency, velocity and action of core particles and we defined $\Omega_{\text{dyn}} = 1/t_{\text{dyn}}$, $v_{\text{dyn}} = L/t_{\text{dyn}}$ and $J_{\text{dyn}} = LV_{\text{dyn}}$, from the dynamical time t_{dyn} of Eq.(18). Let us consider the dissipation rate $\gamma = -\langle \Delta\epsilon/\Delta t \rangle$ of a halo particle with an orbit of order $L/4$ which probes a finite part of the left potential well (i.e. not confined to the small core at $x < R_c$). Its typical frequency, velocity and action are merely $\Omega_{\text{dyn}}, v_{\text{dyn}}$ and J_{dyn} . Since most of the mass (except for an exponentially small fraction, see Eqs.(14)-(15)) is in the core the dissipation rate obtained from Eq.(42) is dominated by core particles J' . Therefore, we have $k/J \sim \zeta_L$ and $k'/J' \sim \zeta_L^3$ hence expression (42) is governed by its second term. Next, using:

$$\frac{df_0}{dJ'} = \Omega' \frac{df_0}{de'} = -\beta \Omega' f_0 \quad (45)$$

for the equilibrium distribution (7) and integrating by parts we obtain:

$$\gamma = \frac{4\pi^2 \beta}{m} \int dJ' f_0(J') \sum_{k,k'=1}^{\infty} |\phi_{k,k'}|^2 k^2 \Omega^2 \delta_D(k\Omega - k'\Omega'). \quad (46)$$

As could be expected, we find that the energy drift $\langle \Delta\epsilon \rangle$ corresponds to a damping term (γ is positive) of order $1/N$. Thus, the high-energy halo particle loses its energy to lower-energy core particles. This is similar to the dynamical friction suffered by a high-speed star moving through an homogeneous background of lower velocity stars [17, 18]. Moreover, the diffusion coefficient $D = \langle (\Delta\epsilon)^2/\Delta t \rangle$ obtained in Eq.(43) and the dissipation coefficient γ are related by:

$$D = \frac{2\gamma}{\beta} = 2\gamma T. \quad (47)$$

Therefore we recover the usual Einstein relation (47) for a halo particle. Next, from the definition (24) we have:

$$\phi_{k,k'} = gm \int_0^\pi \frac{dw}{dw'} \pi^2 |x - x'| \cos(kw) \cos(k'w'). \quad (48)$$

If we approximate each orbit by its first harmonic $x = R \sin(w/2)$ we obtain:

$$\phi_{k,k'} \simeq -\frac{gm}{2\pi} \frac{R'^2}{R} \delta_{k',1} \quad \text{for } k \geq 1, k' \geq 1, R' \ll R. \quad (49)$$

Taking into account the exact orbital trajectory would remove the Kronecker factor $\delta_{k',1}$ (higher k' would contribute) but would not change the scaling gmR'^2/R . Next, from Eq.(27) we see that the action and angle of each core particle in a given realization (i.e. without performing any averaging) are modified by discrete effects

over a time-scale Δt_c of order:

$$\Delta t_c \sim \frac{J}{\dot{J}} \sim \frac{\sqrt{N}}{\Omega_c} \sim \frac{\sqrt{N}}{\zeta_L} t_{\text{dyn}}, \quad (50)$$

whereas for halo particles we obtain:

$$\Delta t_h \sim \sqrt{N} \zeta_L^3 t_{\text{dyn}} \gg \Delta t_c, \quad (51)$$

where we used the scalings (44) and (49). Therefore, we see that the core particles are significantly perturbed over a time-scale which is much smaller than for the halo particles. Then, the resonances between halo and core particles will be detuned over times of order Δt_c during which the trajectory of the halo particle has only suffered small deviations. This means that the core particles act as an external noise characterized by small time-scales with respect to the halo particle. This justifies a Markovian approximation for the behaviour of the halo particle and allows us to write a Fokker-Planck equation [16] for the evolution of the probability distribution $P(\epsilon)$ of its energy:

$$\frac{\partial P}{\partial t} = \frac{\partial}{\partial \epsilon}(\gamma P) + \frac{1}{2} \frac{\partial^2}{\partial \epsilon^2}(D P). \quad (52)$$

The orbit-averaged Fokker-Planck equation (52) clearly separates the slow changes in phase-space coordinates due to encounters from the fast orbital motion in the mean-field potential [18]. Indeed, the dissipation and diffusion coefficients scale as $1/N$ from Eqs.(42)-(43). It is interesting to note that for the OSC model (1) particles which do not cross the test mass do not contribute. This can be checked from Eq.(48) by noting that in such cases the absolute value can be dropped which yields $\phi_{k,k'} = 0$ for $k \neq 0$ and $k' \neq 0$. This is related to the fact that in 1-D gravity the force is merely proportional to the relative number of particles to the left and to the right of the test particle, independently of distances, as seen from Eqs.(1) or (16). Therefore, only particle crossings can lead to fluctuations of the force seen by the test mass. The stationary solution P_{st} of the Fokker-Planck equation (52) is:

$$P_{\text{st}}(\epsilon) \propto \frac{1}{D} e^{-(2\gamma/D)\epsilon}. \quad (53)$$

We can note that this distribution agrees with the statistical equilibrium state “ $n = 2$ ” described by the Maxwellian (7) thanks to Einstein’s relation (47). On the other hand, we must point out that the relaxation of core particles cannot be described by the Fokker-Planck equation (52) because there is no separation of time-scales as in Eqs.(50)-(51) which prevents the use of the Markovian approximation. This also explains why the Einstein relation (47) does not hold for core particles (since we cannot any longer neglect the first term of Eq.(42)). From Eq.(52) we can obtain the mean time τ it takes for a particle starting at energy ϵ_- in the potential well ϕ_0 to reach the maximum potential energy ϵ_+ . It reads [16]:

$$\tau = \int_{\epsilon_-}^{\epsilon_+} d\epsilon e^{F(\epsilon)} \int_{\epsilon_-}^{\epsilon} d\epsilon' \frac{2}{D(\epsilon')} e^{-F(\epsilon')}, \quad (54)$$

with:

$$F(\epsilon) = \int_{\epsilon_-}^{\epsilon} d\epsilon' \frac{2\gamma(\epsilon')}{D(\epsilon')} = \beta(\epsilon - \epsilon_-). \quad (55)$$

Eqs.(54)-(55) clearly show that the escape time is dominated by the time spent at large values of ϵ , that is at large radii of order $L/2$ far from the small core. They give:

$$\tau \sim \frac{2}{\beta^2 D} \left[e^{\beta(\epsilon_+ - \epsilon_-)} - 1 - \beta(\epsilon_+ - \epsilon_-) \right]. \quad (56)$$

On the other hand, the diffusion coefficient (43) can be simplified by first integrating over J' :

$$D = \frac{8\pi^2}{m} \sum_{k,k'=1}^{\infty} \left| \frac{dJ'}{d\Omega'} \right| f_0(J') |\phi_{k,k'}|^2 k' \Omega'^2 \Bigg|_{\Omega'=k\Omega'/k'} . \quad (57)$$

Since $\Omega/\Omega' \sim 1/\zeta_L \ll 1$ the sum over k can now be approximated by an integral over J' which yields:

$$D \simeq \frac{8\pi^2}{m} \sum_{k'=1}^{\infty} \int dJ' f_0(J') |\phi_{k,k'}|^2 \frac{k'^2 \Omega'^2}{\Omega} \Bigg|_{k=k'\Omega'/\Omega} . \quad (58)$$

From the scalings (44) and (49) this gives:

$$D \sim \frac{1}{N \zeta_L^2} \frac{T^2}{t_{\text{dyn}}}. \quad (59)$$

Taking for the energy gap $\Delta\epsilon = \epsilon_+ - \epsilon_-$ the potential barrier $\Delta\Phi = \Delta\phi$ between the bottom of the potential well at $x = 0$ and the maximum at $x = L/2$ we obtain:

$$\begin{aligned} \tau &\sim t_{\text{dyn}} N \zeta_L^2 [e^{\beta\Delta\varphi} - 1 - \beta\Delta\varphi] \\ &\sim t_{\text{dyn}} N \zeta_L^2 \left[\frac{\rho_{\text{max}}}{\rho_{\text{min}}} - 1 - \ln \frac{\rho_{\text{max}}}{\rho_{\text{min}}} \right], \end{aligned} \quad (60)$$

where we used Eq.(8). Thus, at low temperatures we obtain from Eqs.(14)-(15) the asymptotic behaviour:

$$\tau \sim t_{\text{dyn}} N \zeta_L^4 e^{\zeta_L^2/8} \sim t_{\text{dyn}} N \left(\frac{T_{c2}}{T} \right)^2 e^{\pi^2 T_{c2}/2T}, \quad (61)$$

where we used the rescaling (12). From Eq.(60) we can estimate the mass flux from one peak to the other one as:

$$\frac{dM}{dt} = \frac{M}{2t_M} \quad \text{with} \quad \frac{t_M}{t_{\text{dyn}}} = 0.2 \frac{N \zeta_L^2}{2} \left[\frac{\rho_{\text{max}}}{\rho_{\text{min}}} - 1 - \ln \frac{\rho_{\text{max}}}{\rho_{\text{min}}} \right]. \quad (62)$$

Here the factors $M/2$ and $N/2$ translate the fact that only half of the total mass is within each peak whereas the factor 0.2 of order unity has been chosen so as to match the slope of the mass transfer at early times displayed in right panel of Fig. 10, which shows the evolution of a typical system with a transition time $t_{2 \rightarrow \pm 1} \simeq 4.7 \times 10^4 t_{\text{dyn}}$ equal to the mean obtained from 200 numerical

simulations (solid line in right panel of Fig. 8). Then, in order to take into account the acceleration of the mass transfer close to the transition we simply write the mean transition time $t_{2 \rightarrow \pm 1}$ as:

$$t_{2 \rightarrow \pm 1} = \frac{\Delta M}{M/2} t_M \text{ with } \Delta M = (M_L(n=1) - M/2)/4, \quad (63)$$

where $M_L(n=1)$ is the final mass located at $x < L/2$ in the equilibrium state $n = 1$ whereas the factor 4 accounts for the late steepening of the mass transfer estimated from Fig. 10. The transition time (63) is shown as the dashed-lines in Figs. 8-9. We can check that it agrees with numerical simulations and recovers the steep increase obtained at low total energies, as the exponential of the inverse temperature (see Eq.(61)). The departure at higher energies close to the transition T_{c2} is expected since the approach described above was performed in the low-temperature limit $\zeta_L \gg 1$ where the hierarchy (51) holds. Close to T_{c2} one cannot distinguish halo and core particles and one cannot use a Fokker-Planck equation as (52). Besides, Eq.(61) shows that the relaxation time increases linearly with the number of particles N , in agreement with the numerical results shown in Fig. 9. This is different from the relaxation of homogeneous states obtained in the HMF model [20] where the relaxation time was seen to grow faster than N (numerical simulations gave $\sim N^{1.7}$ [8, 24]). However, we must note that Eq.(61) was derived in the low-energy limit where the system is strongly inhomogeneous. Therefore, the physical process involved in the relaxation (the escape of particles from the smallest potential well) is rather different. On the other hand, [25] also found a relaxation time proportional to N for the 1-D gravitational system (which is identical to the OSC model without the reflecting walls and the external potential V). However, using the Fokker-Planck equation derived in [26] for the diffusion in (v, a) space (velocity v and acceleration a) from a Markovian approximation, [25] obtained a Fokker-Planck equation in energy space as in Eq.(52) but without the friction term. Indeed, as seen above the latter arises from the correlations between particles which accumulate over time but these were not considered in [26] which computed the transport coefficients in (v, a) space in the limit of infinitesimal time-steps and next assumed a Markovian evolution. This procedure cannot be applied here since correlations do not decrease exponentially with time (see for instance the cosine dependence in Eqs.(33),(39)) and the dynamics cannot be described as Markovian over time-steps of the order of a few orbital times (which amounts to erase all correlations every few orbital times). Moreover, the dissipation term in Eq.(52) is clearly required by physical consistency to recover the stationary distribution (53) and Einstein's relation.

We can note that halo and core particles are rather strongly coupled in the sense that the dissipation and diffusion coefficients only decrease as a power of the ratio of orbital frequencies Ω'/Ω (through the factors $(R'/R)^2$ in Eq.(49) and $(\Omega'/\Omega)^2$ in Eq.(58)) which gives rise to

the inverse power of ζ_L in Eq.(59). This is significantly different from the coupling in 3D gravity between a small dense core and unbounded scattering particles. In that case the smooth gravitational interaction (for non-zero impact parameter) leads to a coupling and a dissipation which decrease exponentially with the ratio of frequencies [27]. In the case we consider here the large transition time observed at low temperature is not due to exponentially small couplings between halo and core particles. It is merely due to the usual Arrhenius factor $e^{-\Delta\epsilon/T}$ associated with the diffusion through a finite potential barrier. Finally, we can note that our results also apply to any Hamiltonian system with a two-body interaction which shows similar equilibria states. We only need to use the relevant scalings over the temperature T (in our case written in terms of ζ_L).

IV. CONCLUSION

We have studied in this article the relaxation of a 1-D gravitational system (OSC model) which was originally derived from the formation of large-scale structures in cosmology [10, 15, 28]. We have checked that the homogeneous equilibrium state $n = 0$ becomes unstable below the critical energy E_{c1} and exhibits a relaxation to the one-peak state $n = \pm 1$ over a few dynamical times. This is consistent with the fact that the homogeneous state is unstable both from a thermodynamical analysis and from a dynamical mean-field analysis. Therefore, the linear instability of the Vlasov dynamics leads to a violent relaxation to the stable equilibrium $n = \pm 1$ (or to a nearby one-peak state) which develops through a collective dynamical instability.

On the other hand, close to the transition E_{c1} we have found that for moderate numbers of particles ($N = 50$) the fluctuations due to finite N effects are large enough to prevent the system from converging towards a stable equilibrium. Indeed, the system keeps wandering over left and right peak states since it can easily jump from one equilibrium to another one. For larger numbers of particles ($N = 1000$) the fluctuations due to discrete effects are much smaller than the distance (in terms of energy levels or mass ratios) between homogeneous, left and right peak states (unless we go closer to E_{c1}). Then, starting from the homogeneous unstable equilibrium the system wanders again for a long time ($\sim 5000t_{\text{dyn}}$) over left and right peak states but it eventually manages to settle in a stable left or right peak equilibrium.

Finally, at low energies below E_{c2} we have noticed that in some cases the homogeneous state does not relax directly to a left or right peak configuration but first converges over a few dynamical times towards a two-peak state close to equilibrium $n = 2$. Then, the system undergoes a slow collisional relaxation towards a one peak state $n = \pm 1$.

Next, we have investigated the relaxation to thermodynamical equilibrium of the two-peak equilibrium $n = 2$.

As expected, we have found that since this is a stable equilibrium of the mean-field Vlasov dynamics the relaxation involves a slow diffusion process over a time-scale $t_{2 \rightarrow \pm 1}$ which diverges with N . Moreover, after the smallest density peak has lost most of its mass the two-peak configuration (with a high mass ratio) turns dynamically unstable and the system converges to a one-peak state over a few dynamical times. We have estimated analytically the mean transition time $t_{2 \rightarrow \pm 1}$ by describing the slow diffusion of particle energies due to finite N effects through a Fokker-Planck equation. We have found that the friction and diffusion coefficients of halo particles satisfy Einstein's relation and we have obtained a mean transition time of the form $t_{2 \rightarrow \pm 1} \sim N e^{1/T}$ which is proportional to the number of particles and grows at low temperatures. We have checked that this prediction agrees reasonably well with our numerical simulations. The relaxation involves an efficient coupling between the halo particles which extend close to the barrier at $L/2$ and the core particles buried in the density peaks thanks to efficient resonances at high harmonics. Thus, although halo particles have a much smaller orbital frequency than core particles the dissipation and diffusion due to the build-up of correlations and encounters do not vanish exponentially with the ratio of orbital frequencies.

Therefore, we have found that the relaxation of the OSC model proceeds in a fashion similar to some other long-range systems. It first involves a violent relaxation phase governed by dynamical instabilities, where the system converges to stable solutions of the mean-field Vlasov dynamics over a few dynamical times. This is followed by a second much slower collisional relaxation phase where the system goes through a series of quasi-stationary states of the Vlasov dynamics until it reaches the thermal equilibrium. Moreover, we have found that this slow evolution can be followed by another violent relaxation step as the series of quasi-stationary states may lead to an unstable configuration (the least stable eigenvalue increases along the series and eventually becomes positive) which quickly relaxes to a new quasi-stationary solution. Here we note that the slow relaxation of the system as he goes through the series of quasi-stationary states is due to dynamical constraints and not to metastability as for the cases discussed for instance in [29] where the system is trapped in local entropy maxima. On the other hand, the route to thermal equilibrium clearly depends on the initial conditions. Therefore, the relaxation time exhibits a strong dependence on the initial conditions, as shown by the comparison of $t_{0 \rightarrow \pm 1}$ and $t_{2 \rightarrow \pm 1}$ studied in this article.

[1] T. Dauxois, S. Ruffo, E. Arimondo, and M. Wilkens, *Dynamics and thermodynamics of systems with long range interactions* (Lecture Notes in Physics, Springer, aa, 2002).

[2] T. Padmanabhan, Phys. Rep. **188**, 285 (1990).

[3] P. Chavanis, Physica A **361**, 81 (2006).

[4] M. Luwel and G. Severne, A&A **152**, 305 (1985).

[5] T. Tsuchiya, N. Gouda, and T. Konishi, Astrophys. Space Sci. **257**, 319 (1998).

[6] K. Yawn and B. Miller, Phys. Rev. E **68**, 056120 (2003).

[7] D. Lynden-Bell, MNRAS **136**, 101 (1967).

[8] Y. Yamaguchi, J. Barre, F. Bouchet, T. Dauxois, and S. Ruffo, Physica A **337**, 36 (2004).

[9] J. Barre, F. Bouchet, T. Dauxois, S. Ruffo, and Y. Yamaguchi (2005), cond-mat/0511070.

[10] P. Valageas, A&A (2006), astro-ph/0601390.

[11] H. de Vega and J. Siebert, Nucl. Phys. B **707**, 529 (2005).

[12] H. de Vega and J. Siebert, Nucl. Phys. B **726**, 464 (2005).

[13] P. Peebles, *The large scale structure of the universe* (Princeton University Press, Princeton, 1980).

[14] A. Noullez, D. Fanelli, and E. Aurell, Journ. Comp. Phys. **186**, 697 (2003), cond-mat/0101336.

[15] D. Fanelli and E. Aurell, A&A **395**, 399 (2002).

[16] N. van Kampen, *Stochastic Processes in Physics and Chemistry*, 5th ed. (Elsevier, Amsterdam, 2004).

[17] S. Chandrasekhar, ApJ **97**, 255 (1943).

[18] J. Binney and S. Tremaine, *Galactic dynamics* (Princeton University Press, Princeton, 1987).

[19] F. Bouchet, Phys. Rev. E **70**, 036113 (2004).

[20] F. Bouchet and T. Dauxois, Phys. Rev. E **72**, 045103 (2005).

[21] A. Fridman and V. Polyachenko, *Physics of gravitating systems* (Springer Verlag, New York, 1984).

[22] D. Lynden-Bell and A. Kalnajs, MNRAS **157**, 1 (1972).

[23] P. Chavanis (2005), cond-mat/0509767.

[24] D. Zanette and M. Montemurro, Phys. Rev. E **67**, 031105 (2003).

[25] B. Miller, Phys. Rev. E **53**, 4279 (1996).

[26] K. Yawn, B. Miller, and W. Maier, Phys. Rev. E **52**, 3390 (1995).

[27] I. Ispolatov and M. Karttunen, Phys. Rev. E **70**, 026102 (2004).

[28] E. Aurell, D. Fanelli, and P. Muratore-Ginanneschi, Physica D **148**, 272 (2001).

[29] P. Chavanis, A&A **432**, 117 (2005).